Modeling the impact of neuromorphological alterations in Down syndrome on fast neural oscillations

Pau Clusella[1*], Linus Manubens-Gil[2*], Jordi Garcia-Ojalvo[3], Mara Dierssen[3,4,5]

1 Department of Mathematics, Universitat Politècnica de Catalunya, Manresa, Spain
2 New Cornerstone Science Laboratory, SEU-ALLEN Joint Center, Institute for Brain and Intelligence, Southeast University, Nanjing, Jiangsu, China
3 Department of Medicine and Life Sciences, Universitat Pompeu Fabra, Barcelona, Spain
4 Centre for Genomic Regulation (CRG), The Barcelona Institute for Science and Technology (BIST), Barcelona, Spain
5 Center for Biomedical Research in the Network of Rare Diseases (CIBERER), Spain
* pau.clusella@upc.edu
* linusmg@seu.edu.cn

Abstract

Cognitive disorders, including Down syndrome (DS), present significant morphological alterations in neuron architectural complexity. However, the relationship between neuromorphological alterations and impaired brain function is not fully understood. To address this gap, we propose a novel computational model that accounts for the observed cell deformations in DS. The model consists of a cross-sectional layer of the mouse motor cortex, composed of 3000 neurons. The network connectivity is obtained by accounting explicitly for two single-neuron morphological parameters: the mean dendritic tree radius and the spine density in excitatory pyramidal cells. We obtained these values by fitting reconstructed neuron data corresponding to three mouse models: wild-type (WT), transgenic (TgDyrk1A), and trisomic (Ts65Dn). Our findings reveal a dynamic interplay between pyramidal and fast-spiking interneurons leading to the emergence of gamma activity ($\sim$40 Hz). In the DS models this gamma activity is diminished, corroborating experimental observations and validating our computational methodology. We further explore the impact of disrupted excitation-inhibition balance by mimicking the reduction recurrent inhibition present in DS. In this case, gamma power exhibits variable responses as a function of the external input to the network. Finally, we perform a numerical exploration of the morphological parameter space, unveiling the direct influence of each structural parameter on gamma frequency and power. Our research demonstrates a clear link between changes in morphology and the disruption of gamma oscillations in DS. This work underscores the potential of computational modeling to elucidate the relationship between neuron architecture and brain function, and ultimately improve our understanding of cognitive disorders.

Author summary

The structural integrity of individual brain neurons and the intricate networks they form are fundamental to all brain functions, with structural anomalies directly linked to neurological disorders. Deciphering these links is a leading question in developmental disorders such as Down syndrome. Our work sheds light on the pivotal role that the

structure of complex neural systems plays in shaping emergent network activity. In particular, our anatomically informed network modeling enables determining the extent to which specific deficits in neuronal architecture and connectivity perturb oscillatory patterns of activity.

Introduction

Down Syndrome (DS), caused by the trisomy of chromosome 21, is associated with a wide spectrum of cognitive deficits [1], making it the most prevalent form of intellectual disability. Notably, abnormalities in the nervous system of individuals with DS manifest already at the single-neuron level. Mouse models of DS exhibit a significant reduction of dendritic tree branching and spine density when compared to control groups [2–4], features that have also been found in human postmortem tissue [5]. These morphological alterations are believed to play a significant role in the disruption of neural circuitry, ultimately contributing to the cognitive impairments associated with DS. Nevertheless, the precise mechanisms underlying the relationship between microscopic morphological alterations and mesoscopic brain dysfunction remain unknown.

Electrophysiological studies also show abnormal neural synchronicity in DS [6]. In particular, gamma rhythms (~ 40 Hz) appear to be significantly reduced in both awake and anesthetized DS mouse models [7]. Alterations of these fast neural rhythms are not exclusive to DS, and have also been observed in other neuropathologies, such as Alzheimer's disease [8, 9]. Gamma oscillations emerge from the collective activity of neural networks in both the hippocampus and cortex, and have been consistently associated with various cognitive processes, such as decision-making and memory tasks, across different species [10–17].

Thus we hypothesized that there is a direct link between microscopic circuitry abnormalities and functional deficits. However, this relation cannot be tested experimentally due to the presence of confounding factors in animal models. For instance, Ruiz-Mejias et al. [7] also reported a significant reduction of inhibitory connections targeting parvalbumin-positive interneurons in DS. This weakened recurrent inhibition was hinted as a potential cause for the reduction of gamma oscillations using a computational model, but the role of neuromorphological alterations was not explored in that study.

Here we propose a data-driven computational model of a simplified local neural network that incorporates some of the observed neuromorphological changes present in DS mouse models. We selected two different mouse models. The first model is trisomic for about two-thirds of the genes orthologous to human chromosome 21, (Ts65Dn), and is a well-characterized model for studying DS. The second model (TgDyrk1A), overexpresses only the dual-specificity tyrosine phosphorylation-regulated kinase 1A ($DYRK1A$), a gene whose overexpression recapitulates the main neuronal architecture defects and cognitive impairments of the trisomy [18]. By integrating empirical data on dendritic complexity and spine density obtained from wild-type (WT), transgenic (TgDyrk1A), and trisomic mice (Ts65Dn), we construct a simplified cortical-layer structural model representing the synaptic connectivity of a neural network composed of point neurons, including pyramidal and fast-spiking interneurons. Simulations of these neural networks using Izhikevich dynamics [19] provide the functional differences between the three genotypes. Specifically, the model reproduces the deficit in gamma oscillations observed in DS animal models. and allows us to test the role of reduced recurrent inhibition observed in [7]. Moreover, the scalable nature of the modeled morphologies enables us to explore the morphological space. This exploration includes values that do not correspond to specific animal models, allowing us to assess the impact of fabricated topologies on gamma rhythm generation.
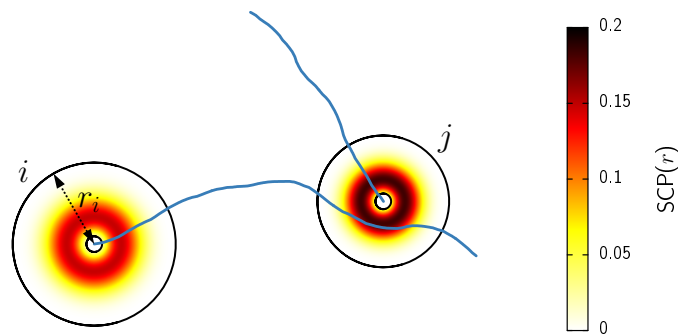
Fig 1. Schematic representation of the neural network topology generation. Small and large black circles represent the neurons' soma and dendritic tree, respectively. The color gradient of the dendritic tree corresponds to the synaptic contact probability of each of the two neurons. Blue curves depict the axons, grown according to a biased random walk. Since the axon of neuron i overlaps with the dendritic tree of neuron j, a synapse might be established. The strength of the synapse depends on the length of the overlap and the value of the SCP along the coincident sites.

Altogether, our study offers new insights into the complex interplay between neural morphology and network-level dynamics, thus contributing to our understanding of neurodevelopmental disorders.

Results

Our model consists of an *in silico* representation of a cross-section of layers II/III of the mouse motor cortex. In this neural network, we considered a total of $N = 3037$ neurons randomly distributed in a 2-dimensional square, with each side measuring $1500\,\mu$m. Details on the model construction, relevant parameters, and their grounding to the literature are outlined in the Methods section, but we briefly summarize the main aspects here.

The main challenge in our computational approach is to represent neural connectivity in a way that integrates single-cell morphology. Following the ideas of previous modeling studies [20, 21], we approach this problem by assuming simplified neuronal shapes paired with synaptic contact probability clouds based on experimental data. Each synthetic neuron is composed of a soma, a dendritic tree with variable size, and an axon. Axons are generated following a biased random walk starting from each neuron's soma (see Fig 1). Whenever there is an intersection between a dendritic tree and an axon, a synapse is established according to a *synaptic contact probability* (SCP). The SCP function quantifies the likelihood of encountering a branch with a spine at a certain radial distance from the soma, denoted as r. Consequently, the SCP is influenced by the unique morphological attributes of each genotype (WT, Ts65Dn, TgDyrk1A).

Synaptic contact probability from morphological data

To model the impact of neuromorphological alterations on the neural network topology in healthy and DS conditions we analyzed 18 individual pyramidal neurons from WT, Ts65Dn, and TgDyrk1A animal models (6 neurons for each genotype, see Methods) to calculate SCP based on single-cell morphology data.

Reconstruction of the analyzed neurons is displayed in Fig 2(a-c). For each cell, we obtained the dendritic branching using a Sholl analysis [22]. The Sholl intersection
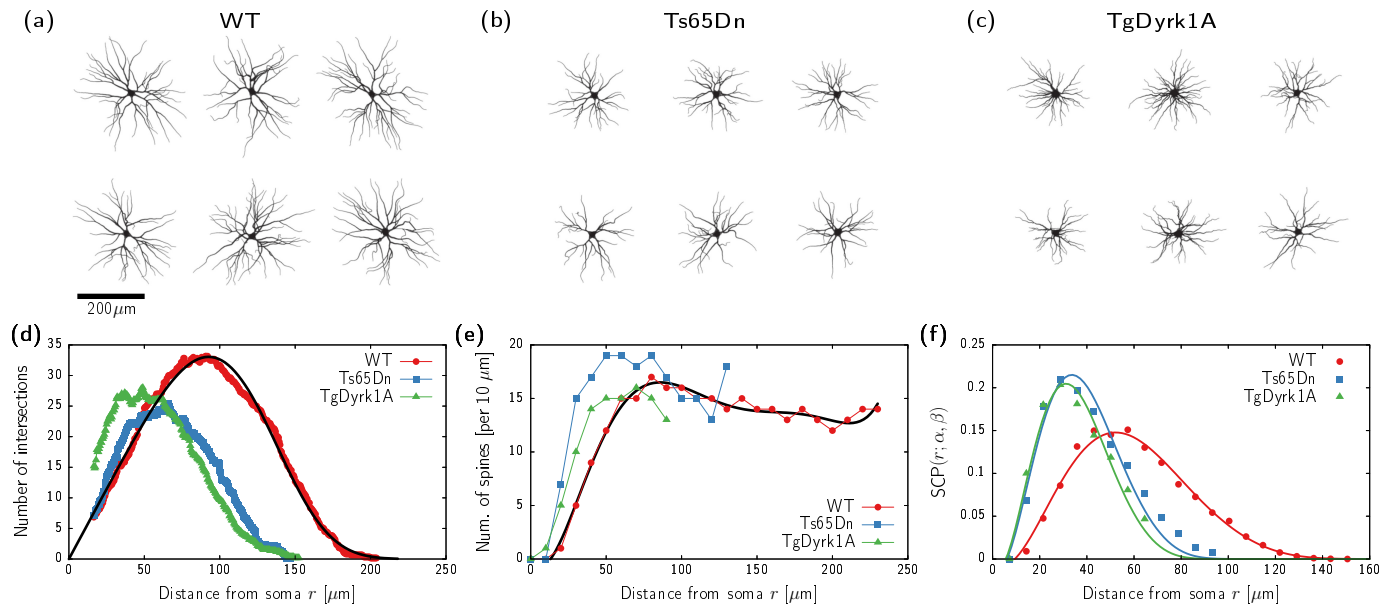
Fig 2. Neuromorphological data and corresponding models. (a-c) Reconstructed neurons for each of the three animal models. (d) Sholl intersectional profile (branch pattern complexity) for the three different genotypes (WT, Ts65Dn and TgDyrk1A). Each dataset corresponds to the average reconstruction of 6 different neurons. Black curve corresponds to fitting Eq (1) to the WT data (see Table 1). (e) Spine density for each different genotype as published in previous literature. The spine numbers are per $10\,\mu$m, thus the distributions are divided by 10 in the fitting procedure. Black curve corresponds to fitting Eq (2) to the WT data (see Table 1). (f) Resulting synaptic contact probability function. Circles, squares, and triangles obtained from the data presented in panels (d) and (e), continuous curves obtained from the nonlinear fitting of Eq. (4) using the rescaling parameters α and β (see Table 2).

profile is obtained by counting the number of dendritic branches at a given distance from the soma and is a key measure of dendritic complexity. Fig 2(d) shows the average number of intersections as a function of the distance from the soma r for each genotype. Neurons corresponding to the pathological conditions display significantly less branch density and shorter dendritic trees than the control condition (WT). Nonetheless, the shape of the branch density distribution, e.g. how branches are distributed or clustered in a particular area, exhibits a consistent similarity among the three cases, with variations primarily attributable to scaling factors. Using the WT case as the reference, we performed a non-linear fitting of the averaged Sholl intersection profile using the function

$$\mathrm{BD}(r) = ax\exp(-bx^4)\,. \tag{1}$$

The choice of this function allows for an appropriate fit of the data with only two free parameters. The black curve in Fig 2(d) depicts the outcome of the fitting, with the resulting function parameters detailed in Table 1.

Next, we consider the dependency of spine density on the distance from the soma. Here we use data previously published in [2,3] (see Fig 2(e)). Again, the maximal spine density remains comparable across trisomic, transgenic, and WT genotypes, but is influenced by the shorter dendritic trees in pathological conditions. We fit the WT

spine density distribution using a 6th degree polynomial

$$\mathrm{SD}(r) = \sum_{j=0}^{6} c_j x^j \; . \tag{2}$$

Table 1 contains the parameter values obtained from the fitting, and the black curve in Fig 2(e) shows the resulting function.

The product of the BD and SD functions provides the average spine density at a certain distance from the soma. These functions assume straight dendrites, whereas these are actually irregularly shaped in nature. Indeed, while the largest distance between a spine and the soma in the WT case is $218\,\mu\mathrm{m}$, using a convex polygon fitting of reconstructed WT neurons, we found an average mean dendritic tree radius of $\overline{R}_{\mathrm{WT}} = 156.30\,\mu\mathrm{m}$ (see Methods). To account for the actual shape of the dendritic tree, we re-scale the radius in the BD and SD functions by a factor $\gamma = 218/156.30$. Finally, we divide by $2\pi r$ to account for the circular shape of the dendritic tree.

Altogether, for a typical WT neuron, the probability of finding a spine at a distance r from the soma is given by

$$\mathrm{SCP}(r) = \frac{\mathrm{BD}(\gamma r)\,\mathrm{SD}(\gamma r)}{2\pi r} \; . \tag{3}$$

This function is depicted in Fig 2(f) (see red continuous curve), together with the morphological data (see red circles).

In order to obtain a SCP distribution for Ts65Dn and TgDyrk1A, we exploit the fact that their spine and branch densities in Fig. 2(d,e) follow a similar shape to the WT case up to scaling factors. Therefore, we consider the following generalization of the SCP:

$$\mathrm{SCP}(r; \alpha, \beta) = \alpha \frac{\mathrm{BD}\left(\frac{\gamma}{\beta}r\right)\mathrm{SD}\left(\frac{\gamma}{\beta}r\right)}{2\pi r} \; . \tag{4}$$

Here, the parameter α determines an overall scaling of the SCP in comparison to the WT, whereas $\beta = \overline{R}/\overline{R}_{\mathrm{WT}}$ provides the ratio of the mean dendritic tree radius in comparison to WT. We fit the expression in Eq. (4) to the data corresponding to Ts65dn and TgDyrk1A (see blue squares and green triangles in Fig 2(c)) with α and β as free parameters. Table 2 contains the resulting values of the neuromorphological parameters, and continuous curves in Fig 2(f) display the resulting shape of the SCP.

The good agreement between the SCP model (Eq. (4)) and the morphological data for the three genotypes substantiates the characterization of single neurons' morphology alterations in DS with only two parameters, α and β.

Parameter	Value
a	0.458
b	$3.39 \cdot 10^{-9}$
c_0	0.0432
c_1	-0.258
c_2	0.0244
c_3	$-4.20 \cdot 10^{-4}$
c_4	$3.12 \cdot 10^{-6}$
c_5	$-1.08 \cdot 10^{-8}$
c_6	$1.44 \cdot 10^{-11}$

Table 1. Results of the nonlinear least-squares fitting of $\mathrm{BD}(r)$ and $\mathrm{SD}(r)$.

Parameter	WT	Ts65Dn	TgDyrk1A
α	1.0	0.937	0.826
β	1.0	0.644	0.597
$\overline{R} = \beta \overline{R}_{\mathrm{WT}}$	156.30	100.66	93.31

Table 2. Parameter values corresponding to the synaptic contact probability obtained from fitting (4) to the data with α and β as free parameters.

Simulations recapitulate disrupted gamma activity in pathological conditions

We generate network topologies corresponding to each of the studied genotypes with the synaptic contact algorithm described in Methods and illustrated in Fig 1. Topology generation parameters are identical for all genotypes (WT, Ts65Dn, TgDyrk1A) except for α and β as described in the previous section (see Table 2). Then, we simulate the dynamics of each neuron using the Izhikevich model with parameters set for regular spiking (pyramidal) and fast-spiking (interneurons) [19] (see Methods). Importantly, each neuron in the network receives an independent train of external excitatory inputs following a Poisson shot process with frequency λ. The codes to generate network topologies and to simulate the network are openly available at github.com/pclus/neuromorphology.

We capture the collective activity of the network by computing the local field potential (LFP) as the average network firing rate (see Methods). In all three neuronal genotypes, the networks robustly produce gamma oscillations, following the paradigmatic pyramidal-interneuron network gamma (PING) mechanism [13, 23, 24]. S1 Movie, S2 Movie, and S3 Movie show such dynamic activity at both single-cell and collective levels. To test the consistency of the results against statistical fluctuations of the topology generation and external input simulation, we generate 10 networks for each of the three neuronal genotypes, and each of them is simulated independently 10 times, resulting in a total pool of 100 time series for each parameter set.

Continuous lines in Fig 3(a) show the average power spectra of the LFP corresponding to each animal model for an input rate $\lambda = 9$ kHz. In all three genotypes, the spectrum shows a clear peak around 40 Hz, with very small deviation across different noise realizations, confirming the robustness of the gamma activity in the model. Nonetheless, the TgDyrk1A and Ts65Dn models display a clear reduction of gamma power compared to the WT case. This decrease in power is paired with a slight decrease in the peak frequency. These results align with empirical observations of reduced gamma activity in PFC of TgDyrk1A mice with compared to WT [7].

Next, we investigate the effects of the external firing rate λ on the network dynamics. Figs 3(b) and (c) show the peak frequency and power, respectively, for the three genotypes upon varying λ (solid lines in the two panels). For all explored values, the three models produce robust oscillatory activity with a peak frequency generally within the gamma range (30-80 Hz). For low values of λ, the network frequency shows similar behavior for all three mouse models, displaying an increase with external input up to $\lambda \approx 12$ kHz. However, for larger values of external input, the monotonic dependence of the frequency on λ breaks down for the DS models. Such decline in frequency observed in TgDyrk1A and Ts65Dn for large λ values is concomitant with an elevation in variability across network realizations, suggesting a lack of uniformity in generating gamma oscillations in the pathological models.

Regarding the power of the neural oscillations (Fig 3(c)), the WT model demonstrates a notably higher gamma amplitude as compared to the DS models for $\lambda > 7$ kHz. These differences in power between genotypes remain mostly unchanged upon increasing λ, although all three models show a reduction of oscillatory coherence
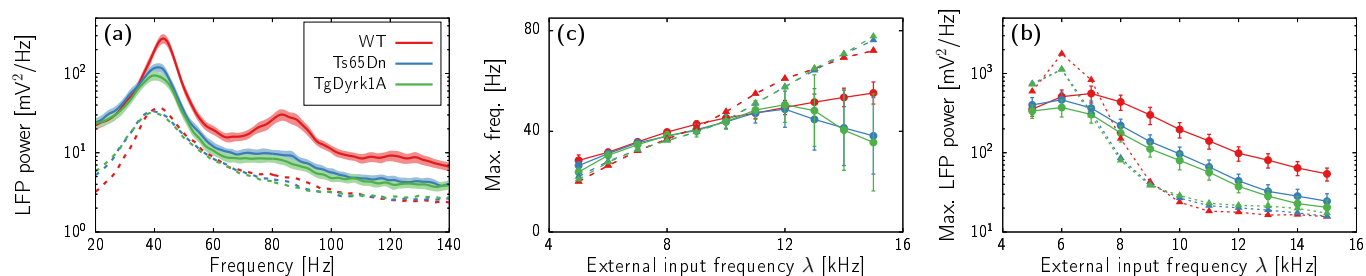
Fig 3. Neuronal network activity. (a) Power spectrum of LFP signals for an input frequency of $\lambda = 9$ spikes/ms. Each curve corresponds to the average of 100 spectra corresponding to 10 independent realizations of the noise for 10 different topologies. Shaded regions indicate the standard deviation among the samples. Red, blue, and green correspond to the morphological parameters of the WT, Ts65Dn, and TgDyrk1A cases, respectively (see Table 2). Dashed lines correspond to simulations with recurrent inhibitory synapses reduced to 0.3 of the original value. (b,c) Location of the peak power in the LFP power spectra (b) and corresponding power (c) obtained for different values of the external firing rate λ. Circles and continuous lines indicate results using the default network parameters. Triangles and dashed lines correspond to the results of the network with reduced recurrent inhibition, as in panel a. Error bars indicate the standard deviation. Each symbol corresponds to 100 simulations (10 simulations for 10 different topology realizations).

as the external input increases. Overall, the scenario remains similar to that displayed in Fig 2(a), and reproduces experimental findings observed in electrophysiology studies of the TgDyrk1A model [7].

Reduced recurrent inhibition might increase or reduce oscillatory activity

Histological analysis of TgDyrk1A and WT mice cortex shows a significant reduction of the inhibitory synapses acting upon interneurons in the DS model [7]. We expect this to influence the network dynamics, since parvalbumin-positive interneurons are known to modulate gamma activity in the cortex [13, 14, 24]. Moreover, recurrent inhibition, one of the key factors involved in fast collective activity [25], was probably a leading cause of the gamma impairment in the DS model [7] given the reduction of GABAergic contacts among interneurons .

In this section, we test the effect of reduced recurrent inhibition in our model. While *in vivo*, this perturbation of the network balance only occurs for DS animals, we deliberately test the effects of disrupted inhibition in all three genotypes. This allows us to compare the effects of morphology alterations and reduced inhibition separately, both of which coexist in DS animal models.

Dashed lines in Fig 3(a) show the average power spectral density (PSD) obtained from simulations in networks with inhibitory-to-inhibitory synaptic strength reduced to 30% for $\lambda = 9$ kHz. While the three genotypes still exhibit a prominent peak around 40 Hz, there is a substantial decrease in activity across all frequency bands when contrasted with the unperturbed models. Significantly, the distinctions in power between WT and DS models vanish, resulting in nearly identical spectra for all three.

Once more, we test the soundness of this scenario upon changing λ. Dashed lines and triangles in Fig 3(b) show the peak frequency for the models with weakened recurrent GABAergic contacts. For low values of the external input, the main frequency of oscillation remains close to the unperturbed models. Moreover, disrupted inhibition

163
164
165

166
167

168
169
170
171
172
173
174

175
176
177
178
179

180
181
182
183
184
185

186
187
188
189

rescues the drop in gamma frequency of the DS models reported in the previous section. Indeed, with higher values of λ all three genotypes exhibit faster oscillatory activity compared to their respective unperturbed models, with no discernible distinctions between the three genotypes.

The stimulating effect of decreased recurrent inhibition on the oscillatory frequency within the DS models differs from its effects on peak power. Dashed lines and triangles in 3(c) show two different scenarios depending on whether the external input is smaller or larger than $\lambda \approx 7$ kHz. With lower external activity levels, disrupted recurrent inhibition enhances oscillatory power, with the WT model consistently exhibiting greater power than the DS models. Conversely, for higher external activity levels, the power of the three modified models rapidly declines below the levels of the default models, with all three genotypes reaching a plateau for $\lambda > 10$ kHz. In this range, no substantial differences in power are discernible among the three genotypes. Furthermore, within this range, the impact of disrupted excitation-inhibition balance on gamma power in the WT appears to be twofold compared to the drop of gamma between the unperturbed WT and DS models. Since frequencies above 40 Hz require $\lambda > 9$ kHZ (Fig 3(b)), these results suggest that reducing recurrent inhibition notably impedes gamma synchronicity, in agreement with [7].

The abrupt reduction in peak power in the disrupted networks corresponds to a transition from a highly synchronized state to a regime in which neurons fire irregularly, while still exhibiting some degree of collective synchronous behavior. These two forms of gamma activity have been identified in previous computational studies and are usually referred to as *strong* and *weak* gamma, respectively [26, 27]. The sensitivity of the network rhythmicity on the external input λ in the perturbed models highlights the importance of recurrent inhibition to obtain robust gamma rhythms in cortical neural networks.

Parameter exploration

The unified SCP (Eq (4)) function derived from the morphological data for the three animal models enables the investigation of the network activity generated by hypothetical neuron morphologies. In this context, we explore the influence of the spine density (α) and dendritic tree size (β) on the power and frequency of the gamma rhythm.

Figure 4 shows the outcome of the LFP signal obtained from numerical simulations in network topologies generated with specific values of the scaling parameters for the mean dendritic tree β and synaptic contact probability α. The peak of the gamma activity is observed at higher frequencies for networks with low values of α and high values of β. Conversely, the power of such gamma activity becomes larger when both morphological parameters are high. This dual relationship highlights that there is no specific region within the morphological space where both frequency and power can be maximized concurrently. Instead, the emergence of these fast oscillations is driven by the topological features of the networks in a nonlinear manner.

When using the exact values of the animal models in this exploration, it becomes evident that the most prominent difference between the DS and the WT is given by a substantial reduction of the parameter β. This implies that the size of the dendritic tree exerts a pivotal influence on the gamma abnormalities when compared with the reduction of the SCP parameter α. Consequently, our computational results indicate that the gamma impairment in DS models is primarily attributed to the loss of synaptic connections among neurons rather than a decline in the overall strength of these connections.
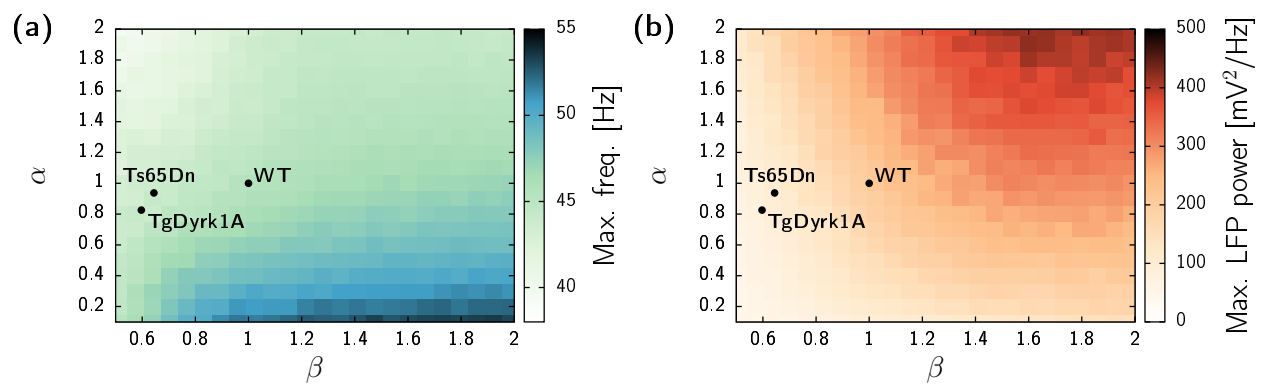
Fig 4. Network activity dependence on the morphological parameters showing the frequency peak of the gamma rhythm (a) and corresponding LFP power (b). Results from numerical simulations of networks for external input $\lambda = 10$ kHz. Each pixel of the heatmap corresponds to the average of results obtained with 10 different network topologies, each simulated with 10 different realizations of the noise. Parameters corresponding to the studied genotypes are marked with black circles for reference.

Discussion

In this study, we aimed to explore the interplay between neuromorphological alterations and network dynamics in DS, using a data-driven computational model. Our findings provide compelling evidence that the incorporation of empirical data on dendritic complexity and spine density into the model enables the faithful replication of the reduction in gamma oscillations documented in DS animal models [7]. These results strongly indicate that the neuromorphological changes observed in DS are pivotal contributors to the disruption of gamma activity, providing valuable insights into the underlying mechanisms of network dynamics associated with DS.

An important challenge of this work has been to integrate single-cell morphology data into the generation of the neural network architecture. Few studies include morphology in neural network topology, and the options vary based on the desired biological realism: from sophisticated cloning of reconstructed morphologies paired with touch-detection rules [28–30], to generating random networks based mostly on axo-dendritic overlap [20, 31]. A mid-way approach consists of defining a probability region based on different morphological parameters [21, 32, 33].

Here we took this intermediate route by incorporating a synaptic contact probability (SCP) function into the model developed in [20]. Through an analysis of single-cell morphology data, we devised a quantitative model for the SCP that integrates dendritic complexity and spine density of different mouse models. Remarkably, our findings demonstrate that the three genotypes examined in this study (WT, trisomic, and single-gene transgenic TgDyrk1A) can be accurately represented by a single SCP function, with scaling factors accounting for their distinct characteristics. This result allowed us to explore the broader morphological landscape beyond the confines of specific animal models.

The simulations conducted in the study demonstrate the influence of diminished recurrent inhibition on network dynamics. The reduction of inhibitory connections, particularly those targeting parvalbumin-positive interneurons, previously reported in DS animal models [7], has been proposed as a potential cause for the observed reduction in gamma oscillation. The model's implementation of reduced recurrent inhibition successfully reproduces the effects on gamma activity, underscoring its pivotal role in modulating network dynamics. Notably, perturbing excitation-inhibition balance rescues

the drop in frequency in DS models but concurrently diminishes oscillatory power. These results align with previous empirical and modeling studies identifying recurrent inhibition as a key ingredient for the emergence of gamma oscillations [14, 24, 25, 34–36].

Furthermore, the study explores the morphological parameter space and demonstrates that there is no single regime in which both frequency and power of gamma oscillations can be maximized. Moreover, the reduction in dendritic tree size (β) appears to be a major factor contributing to the gamma abnormalities in DS, while the reduction in synaptic contact probability (α) plays a secondary role.

In summary, the data-driven computational model presented in this study successfully integrates neuromorphological alterations observed in DS animal models and reproduces the reduction in gamma oscillations. The findings support the notion that microscopic circuitry abnormalities contribute to the disruption of network dynamics in DS. The model provides a controlled framework to explore the impact of morphology alterations and elucidate their role in network synchronicity.

Model limitations

Our data-driven computational approach relies on several modeling assumptions that should be taken into account when drawing biological conclusions from the results. One major simplification pertains to the morphological model for network topologies, which simplifies neuronal shapes and may not fully capture the diversity and intricacy of real morphologies. Furthermore, the axon growth model doesn't consider the precise axon terminal locations.

Another aspect is the dynamical model employed for the simulations. Here we considered idealized point neurons, which are simplified models that disregard the influence of detailed structures, such as dendrites and axons, on the dynamics of the cell. While these simplifications facilitate easier analysis and interpretation, they may not fully capture the effects that morphology can have on the system dynamics. To this end, compartmental models could allow the incorporation of specific relations such as the effects of smaller dendritic trees on the synaptic delays.

Despite these limitations, our data-driven computational model is an important milestone in understanding the importance of neuromorphological alterations in neurodevelopmental diseases. Further work should allow us to improve and further validate our assumptions based on empirical data, as well as focus on other brain areas which are known to be also affected in DS, such as the hippocampus.

Methods

Data gathering

We used previously published single-neuron 2D tracings of cortical layer II/III pyramidal neurons. Those were traced as part of previous studies of our team, following experimental procedures detailed in [37–39]. Briefly, cells were injected with Lucifer Yellow, immuno-stained with a biotinylated secondary antibody and biotin–horseradish peroxidase complex. Tissue sections were imaged with brightfield microscopy and traced using camera lucida microscope attachment. Specifically, the details for the tracing of WT and Ts65Dn neurons can be found at [2], and those for TgDyrk1A neurons can be found at [3]. We did not find differences in neuronal morphology between the WT strains of trisomic and transgenic mice, and thus we consider WT parameters to be the same for the two DS mouse models, thus allowing comparisons among the three genotypes. All data used in this study is openly available at github.com/pclus/neuromorphology.

Topology generation

The generation of the network topology has been largely inspired by the model developed by Orlandi et. al. [20]. We included substantial modifications to their proposal to account for specific morphological variants of single neurons. A C code of the resulting algorithm is openly available at github.com/pclus/neuromorphology.

Using a full 3D representation of the cortical layer II/III with realistic neuronal densities is not possible due to computational limitations [20, 40]. Thus we considered a thin 2-dimensional cross-section of the cortical layer with a thickness of a single cell soma, $16\,\mu$m.

The neuronal density of the synthetic circuit is set to 1350 neurons/mm^2, obtained by multiplying the neuronal density in the 3D layer by the width of the thin layer modeled. Based on this assumption, we placed randomly $N = 3037$ neurons in a 2-dimensional square with a side length of 1.5 mm. To mitigate the effects of imposing a too-small spatial domain, we provided the circuit with periodic boundary conditions. The spatial resolution of the *in silico* layer is 1 μm.

In the model, each neuron has three components: the soma, the dendritic tree, and the axon (see Fig 1 for a schematic representation). All neurons have identical soma, which are modeled as circles of radius $R_S = 16$ μm. The center of each neuron's soma is randomly distributed on the 2-dimensional layer, and overlapping somas are not allowed. The dendritic tree of each neuron is also modeled as a circle, but in this case, we considered variability among neurons. The radius of each neuron's dendritic tree is a random number drawn from a Gaussian distribution with mean $\overline{R}$ and standard deviation $\sigma = 40$. The mean dendritic tree radius $\overline{R}$ is one of the main control parameters of the study. As explained in the Results section, we use the WT mean dendritic tree radius $\overline{R}_{\mathrm{WT}}$ as a reference. We measured this quantity by calculating the 2D convex hull of the reconstructed WT dendritic trees. Specifically, we used the "boundary" function in MATLAB with shrink factor $s = 0$. To obtain the mean radius we assumed that the area obtained with the convex hull forms a circle for each tree.

The axon is modeled as a biased random walk starting from the center of the soma with a random direction. After it has grown $10\,\mu$m, it modifies direction by θ degrees, where θ is a random variable chosen from a Gaussian distribution with zero mean and standard deviation $\sigma = \pi/30$ radians. The total length of each axon is obtained from a Rayleigh distribution with mean $\bar{l} = 500\,\mu$m. This mean axon length has been chosen to simulate only local horizontal connections (given by the local axonal tree in layers II/III), following experimental observations in the mouse M2 cortical layer II/III [40], and disregarding horizontal patchy connections, connections between cortical layers and interhemispheric projections.

If the axon of neuron i overlaps the dendritic tree (but not the soma) of neuron j, then a synapse is established with a probability p that depends on the distance r from the overlap point to the neuron's j soma. Such dependency is given by the function $p = \mathrm{SCP}(r; \alpha, \beta)$ where α and β are parameters that depend on the morphological variables. In particular, α is the ratio between the synaptic contact probability of each mouse model and the wild-type (WT) value, and β is the ratio between the dendritic tree radius of each mouse model and WT, i.e., $\beta = \overline{R}/R_{\mathrm{WT}}$ where $\overline{R}_{\mathrm{WT}} = 156.30\,\mu$m is the mean dendritic tree radius of a WT neuron. The derivation of the synaptic contact probability function $\mathrm{SCP}(r)$ and the values of α and β for the different animal models are detailed in the Results section.

Each grid square presenting an overlap between an axon and a dendritic tree can generate a synapse, thus each pair of neurons might have multiple, in some cases several, synapses. In other words, the resulting architecture of connections among neurons is a directed weighted network given by the weight matrix $\boldsymbol{W} = (w_{jk})$. Autapses are not allowed.

Neuronal dynamics

Several models for spiking neuron dynamics exist in the literature. Here we use the model proposed in [19], due to its apt trade-off between dynamical richness and computational efficiency. The C code used to simulate the network dynamics is openly available at github.com/pclus/neuromorphology.

The dynamics of the j-th neuron in the network is ruled by the following ordinary differential equations,

$$\dot{v}_j = 0.04v_j^2 + 5v_j + 140 - w_j + I_j^{\text{AMPA}} + I_j^{\text{GABA}} + I_j^{\text{ext}} \tag{5}$$

$$\dot{w}_j = a(bv_j - w_j) \tag{6}$$

where v_j is the membrane voltage potential, and w_j is a recovery variable accounting for the dynamics of the different ion channels. When the voltage of neuron j reaches a threshold of $v^{(\text{thr})} = 30$, the neuron emits a spike and the voltage is reset to $v_j \leftarrow c$, whereas $w_j \leftarrow w_j + d$. Upon tuning the system parameters a, b, and d, one can obtain different dynamical behaviors for each neuron. Here we focus on Regular Spiking (RS) for pyramidal neurons and Fast Spiking (FS) for interneurons [19]. Table 3 indicates the numerical value for the parameters corresponding to each neuron type.

The voltage of each neuron is influenced by the synaptic inputs coming from the excitatory neurons of the network, I_j^{AMPA}, inhibitory neurons I_j^{GABA}, and glutamatergic inputs coming from outside the network, I^{ext}. In all cases, these inputs have the form

$$I_j^{\text{syn}} = g_j^{\text{syn}}(t - \tau_0)(v_R^{\text{syn}} - v_j) . \tag{7}$$

with v^{syn} being a reversal potential and g_j^{syn} is a time-dependent conductance, and $\tau_0 = 1$ ms is a fixed synaptic delay. Upon receiving a spike, the neurotransmitter-activated ion channels open and close following an exponential decay. For the recurrent AMPA and GABA connectivities this reads

$$g_j^{\text{syn}}(t) = g^{\text{syn}} \sum_{k=1}^{N} w_{jk} \sum_{m} e^{(t-t_m^{(k)})/\tau^{\text{syn}}} H(t - t_m^{(k)}) \tag{8}$$

where $\mathbf{W} = (w_{jk})$ is the adjacency matrix of the network, $t_k^{(m)}$ is the time at which neuron k emitted its m-th spike, H is the Heaviside step function, τ_{syn} is the decay time, g^{syn} is the strength of the synapse. The incoming signals from outside of the modeled layer consist of excitatory exponential pulses only

$$g_j^{\text{ext}}(t) = g_{\text{ext}} \sum_{m} e^{(t-t_m)/\tau^{\text{ext}}} H(t - t_m) .$$

The spiking times t_m are drawn from a Poissonian shot process with frequency λ. We use λ as the main control parameter to test the oscillatory response of the network. Values for g^{syn}, τ^{syn}, and v_R^{syn} for the three synaptic types are given in Table 4.

Finally, in order to capture the network activity, we model the local field potential (LFP) as the network average firing rate (with time bins of 0.1 ms):

$$\text{LFP}(t) = \frac{1}{N} \sum_{m=1}^{N} \sum_{m} \left[H(t - t_m^{(k)}) - H(t - t_m^{(k)-0.1}) \right] . \tag{9}$$

We opted to use the firing rate as a proxy to capture the actual network activity in our model. Other options, which are based on the AMPA and GABA currents of the network, could be susceptible to parameter changes such as when we model disrupted networks by reducing g^{GABA} targeting inhibitory neurons. Power Spectral Density of LFP time series have been computed using the GNU Scientific Library [41] by first applying a fast Fourier transform algorithm and then reducing the noise in the spectra through a Gaussian filter.

Parameter	Pyramidal (RS)	Interneuron (FS)
a	0.02	0.1
b	0.2	0.2
c	-65	-65
d	8	2

Table 3. Values of the system parameter to display regular spiking for excitatory neurons, and fast-spiking for inhibitory neurons.

	g^{syn}	τ^{syn}	v_R^{syn}
AMPA	0.006 mS	4 ms	0
GABA	0.720 mS	2 ms	-70
External AMPA	0.008 mS	4 ms	0

Table 4. Values of the synaptic strength g^{syn}, decay times τ^{syn}, and reversal potential v_R^{syn} for the different neurotransmitters.

References

1. Lott IT, Dierssen M. Cognitive Deficits and Associated Neurological Complications in Individuals with Down's Syndrome. The Lancet Neurology. 2010;9(6):623–633. doi:10.1016/S1474-4422(10)70112-5.

2. Dierssen M. Alterations of Neocortical Pyramidal Cell Phenotype in the Ts65Dn Mouse Model of Down Syndrome: Effects of Environmental Enrichment. Cerebral Cortex. 2003;13(7):758–764. doi:10.1093/cercor/13.7.758.

3. Martinez de Lagran M, Benavides-Piccione R, Ballesteros-Yanez I, Calvo M, Morales M, Fillat C, et al. Dyrk1A Influences Neuronal Morphogenesis Through Regulation of Cytoskeletal Dynamics in Mammalian Cortical Neurons. Cerebral Cortex. 2012;22(12):2867–2877. doi:10.1093/cercor/bhr362.

4. Dierssen M, Sierra C, Sabariego M, Fernández-Blanco A, Cruciani S, Zamora-Moratalla A, et al. The lncRNA Snhg11, a New Candidate Contributing to Neurogenesis, Plasticity and Memory Deficits in Down Syndrome. In Review; 2023.

5. Marin-Padilla M. Pyramidal Cell Abnormalities in the Motor Cortex of a Child with Down's Syndrome. A Golgi Study. Journal of Comparative Neurology. 1976;167(1):63–81. doi:10.1002/cne.901670105.

6. Ruiz-Mejias M. Outer Brain Oscillations in Down Syndrome. Frontiers in Systems Neuroscience. 2019;13:17. doi:10.3389/fnsys.2019.00017.

7. Ruiz-Mejias M, Martinez de Lagran M, Mattia M, Castano-Prat P, Perez-Mendez L, Ciria-Suarez L, et al. Overexpression of *Dyrk1A* , a Down Syndrome Candidate, Decreases Excitability and Impairs Gamma Oscillations in the Prefrontal Cortex. The Journal of Neuroscience. 2016;36(13):3648–3659. doi:10.1523/JNEUROSCI.2517-15.2016.

8. Verret L, Mann EO, Hang GB, Barth AMI, Cobos I, Ho K, et al. Inhibitory Interneuron Deficit Links Altered Network Activity and Cognitive Dysfunction in Alzheimer Model. Cell. 2012;149(3):708–721. doi:10.1016/j.cell.2012.02.046.

9. Mably AJ, Colgin LL. Gamma oscillations in cognitive disorders. Current opinion in neurobiology. 2018;52:182–187.

10. Ward LM. Synchronous neural oscillations and cognitive processes. Trends in cognitive sciences. 2003;7(12):553–559.

11. Buzsáki G. Rhythms of the Brain. Oxford University Press; 2006.

12. Hanks TD, Summerfield C. Perceptual decision making in rodents, monkeys, and humans. Neuron. 2017;93(1):15–31.

13. Whittington MA, Cunningham MO, LeBeau FEN, Racca C, Traub RD. Multiple Origins of the Cortical Gamma Rhythm. Developmental Neurobiology. 2011;71(1):92–106. doi:10.1002/dneu.20814.

14. Buzsáki G, Wang XJ. Mechanisms of Gamma Oscillations. Annual Review of Neuroscience. 2012;35(1):203–225. doi:10.1146/annurev-neuro-062111-150444.

15. Başar E. A Review of Gamma Oscillations in Healthy Subjects and in Cognitive Impairment. International Journal of Psychophysiology. 2013;90(2):99–117. doi:10.1016/j.ijpsycho.2013.07.005.

16. Hansen BJ, Dragoi V. Adaptation-Induced Synchronization in Laminar Cortical Circuits. Proceedings of the National Academy of Sciences. 2011;108(26):10720–10725. doi:10.1073/pnas.1102017108.

17. Brunet NM, Bosman CA, Vinck M, Roberts M, Oostenveld R, Desimone R, et al. Stimulus Repetition Modulates Gamma-Band Synchronization in Primate Visual Cortex. Proceedings of the National Academy of Sciences. 2014;111(9):3626–3631. doi:10.1073/pnas.1309714111.

18. Martínez de Lagrán M, Altafaj X, Gallego X, Martí E, Estivill X, Sahún I, et al. Motor phenotypic alterations in TgDyrk1a transgenic mice implicate DYRK1A in Down syndrome motor dysfunction. Neurobiology of Disease. 2004;15(1):132–142. doi:https://doi.org/10.1016/j.nbd.2003.10.002.

19. Izhikevich EM. Simple model of spiking neurons. IEEE Transactions on Neural Networks. 2003;14(6):1569–1572. doi:10.1109/TNN.2003.820440.

20. Orlandi JG, Soriano J, Alvarez-Lacalle E, Teller S, Casademunt J. Noise focusing and the emergence of coherent activity in neuronal cultures. Nature Physics. 2013;9(9):582–590. doi:10.1038/nphys2686.

21. Gandolfi D, Mapelli J, Solinas S, De Schepper R, Geminiani A, Casellato C, et al. A Realistic Morpho-Anatomical Connection Strategy for Modelling Full-Scale Point-Neuron Microcircuits. Scientific Reports. 2022;12(1):13864. doi:10.1038/s41598-022-18024-y.

22. Sholl DA. Dendritic Organization in the Neurons of the Visual and Motor Cortices of the Cat. Journal of Anatomy. 1953;87(4):387–406.

23. Brunel N. Dynamics of Sparsely Connected Networks of Excitatory and Inhibitory Spiking Neurons. Journal of Computational Neuroscience. 2000;8(3):183–208. doi:10.1023/A:1008925309027.

24. Wang XJ. Neurophysiological and Computational Principles of Cortical Rhythms in Cognition. Physiological Reviews. 2010;90(3):1195–1268. doi:10.1152/physrev.00035.2008.

25. Bartos M, Vida I, Jonas P. Synaptic Mechanisms of Synchronized Gamma Oscillations in Inhibitory Interneuron Networks. Nature Reviews Neuroscience. 2007;8(1):45–56. doi:10.1038/nrn2044.

26. Börgers C, Epstein S, Kopell NJ. Background Gamma Rhythmicity and Attention in Cortical Local Circuits: A Computational Study. Proceedings of the National Academy of Sciences. 2005;102(19):7002–7007. doi:10.1073/pnas.0502366102.   475 476 477

27. Lee S, Jones SR. Distinguishing Mechanisms of Gamma Frequency Oscillations in Human Current Source Signals Using a Computational Model of a Laminar Neocortical Network. Frontiers in Human Neuroscience. 2013;7. doi:10.3389/fnhum.2013.00869. 478 479 480 481

28. Reimann MW, King JG, Muller EB, Ramaswamy S, Markram H. An Algorithm to Predict the Connectome of Neural Microcircuits. Frontiers in Computational Neuroscience. 2015;9. doi:10.3389/fncom.2015.00120. 482 483 484

29. Markram H, Muller E, Ramaswamy S, Reimann MW, Abdellah M, Sanchez CA, et al. Reconstruction and Simulation of Neocortical Microcircuitry. Cell. 2015;163(2):456–492. doi:10.1016/j.cell.2015.09.029. 485 486 487

30. Udvary D, Harth P, Macke JH, Hege HC, De Kock CPJ, Sakmann B, et al. The Impact of Neuron Morphology on Cortical Network Architecture. Cell Reports. 2022;39(2):110677. doi:10.1016/j.celrep.2022.110677. 488 489 490

31. Hjorth JJJ, Kozlov A, Carannante I, Frost Nylén J, Lindroos R, Johansson Y, et al. The Microcircuits of Striatum in Silico. Proceedings of the National Academy of Sciences. 2020;117(17):9554–9565. doi:10.1073/pnas.2000671117. 491 492 493

32. Pyka M, Klatt S, Cheng S. Parametric Anatomical Modeling: A Method for Modeling the Anatomical Layout of Neurons and Their Projections. Frontiers in Neuroanatomy. 2014;8. doi:10.3389/fnana.2014.00091. 494 495 496

33. Casali S, Marenzi E, Medini C, Casellato C, D'Angelo E. Reconstruction and Simulation of a Scaffold Model of the Cerebellar Network. Frontiers in Neuroinformatics. 2019;13:37. doi:10.3389/fninf.2019.00037. 497 498 499

34. Whittington MA, Traub RD, Jefferys JGR. Synchronized oscillations in interneuron networks driven by metabotropic glutamate receptor activation. Nature. 1995;373(6515):612–615. doi:10.1038/373612a0. 500 501 502

35. Brunel N, Hakim V. Fast Global Oscillations in Networks of Integrate-and-Fire Neurons with Low Firing Rates. Neural Computation. 1999;11(7):1621–1671. doi:10.1162/089976699300016179. 503 504 505

36. Whittington MA, Traub RD, Kopell N, Ermentrout B, Buhl EH. Inhibition-based rhythms: experimental and mathematical observations on network dynamics. International Journal of Psychophysiology. 2000;38(3):315–336. doi:https://doi.org/10.1016/S0167-8760(00)00173-2. 506 507 508 509

37. Buhl EH, Schlote W. Intracellular Lucifer Yellow Staining and Electron Microscopy of Neurones in Slices of Fixed Epitumourous Human Cortical Tissue. Acta Neuropathologica. 1987;75(2):140–146. doi:10.1007/BF00687074. 510 511 512

38. Einstein G. Intracellular Injection of Lucifer Yellow into Cortical Neurons in Lightly Fixed Sections and Its Application to Human Autopsy Material. Journal of Neuroscience Methods. 1988;26(2):95–103. doi:10.1016/0165-0270(88)90157-4. 513 514 515

39. Elston GN, Pow DV, Calford MB. Neuronal Composition and Morphology in Layer IV of Two Vibrissal Barrel Subfields of Rat Cortex. Cerebral Cortex. 1997;7(5):422–431. doi:10.1093/cercor/7.5.422. 516 517 518

40. Voges N, Schüz A, Aertsen A, Rotter S. A Modeler's View on the Spatial Structure of Intrinsic Horizontal Connectivity in the Neocortex. Progress in Neurobiology. 2010;92(3):277–292. doi:10.1016/j.pneurobio.2010.05.001.

41. Galassi M, Gough B. GNU Scientific Library: Reference Manual. Network Theory; 2003.

Supporting information

S1 Movie   Simulation of the model corresponding to WT morphology. Top: spatial representation of the cortex slice model. Each circle represents a neuron, whose spikes are marked with red (excitatory neurons) and blue (inhibitory neurons) for a short time interval. Bottom: Time series of the average firing rate of excitatory (red) and inhibitory (blue) neurons. Simulation parameters as in Fig 3(a) ($\lambda = 9$ kHz).

S2 Movie   Simulation of the model corresponding to Ts65Dn morphology. Top: spatial representation of the cortex slice model. Each circle represents a neuron, whose spikes are marked with red (excitatory neurons) and blue (inhibitory neurons) for a short time interval. Bottom: Time series of the average firing rate of excitatory (red) and inhibitory (blue) neurons. Simulation parameters as in Fig 3(a) ($\lambda = 9$ kHz).

S3 Movie   Simulation of the model corresponding to TgDyrk1A morphology. Top: spatial representation of the cortex slice model. Each circle represents a neuron, whose spikes are marked with red (excitatory neurons) and blue (inhibitory neurons) for a short time interval. Bottom: Time series of the average firing rate of excitatory (red) and inhibitory (blue) neurons. Simulation parameters as in Fig 3(a) ($\lambda = 9$ kHz).